HHS Public Access

Author manuscript

Magn Reson Med. Author manuscript; available in PMC 2021 February 19.

Published in final edited form as:

Magn Reson Med. 2020 December ; 84(6): 3246–3255. doi:10.1002/mrm.28388.

Ultrashort Echo Time Quantitative Susceptibility Mapping (UTE-QSM) for Detection of Hemosiderin Deposition in Hemophilic Arthropathy: a Feasibility Study

Hyungseok Jang[1], **Annette von Drygalski**[2], **Jonathan Wong**[1], **Jenny Y Zhou**[2], **Peter Aguero**[2], **Xing Lu**[1], **Xin Cheng**[3], **Scott T Ball**[4], **Yajun Ma**[1], **Eric Y Chang**[5,1], **Jiang Du**[1,*]

[1]Department of Radiology, University of California San Diego, San Diego, CA, United States

[2]Division of Hematology-Oncology, Department of Medicine, University of California San Diego, San Diego, CA, United States

[3]Department of Histology and Embryology, Medical College, Jinan University, Guangzhou, China

[4]Orthopedic Surgery, University of California San Diego, San Diego, CA, United States

[5]Radiology Service, Veterans Affairs San Diego Healthcare System, San Diego, CA, United States

Abstract

Purpose: The purpose of this study was to investigate the feasibility of ultrashort echo time quantitative susceptibility mapping (UTE-QSM) for assessment of hemosiderin deposition in the joints of hemophilic patients.

Methods: The UTE-QSM technique was based on three sets of dual-echo 3D UTE Cones data acquired with TEs of 0.032/2.8, 0.2/3.6, and 0.4/4.4 ms. The images were processed with Iterative Decomposition of water and fat with Echo Asymmetry and Least-squares estimation (IDEAL) to estimate the B_0 field map in the presence of fat. Then, the projection onto dipole field algorithm was applied to acquire a local field map generated by tissues, followed by application of the morphology-enabled dipole inversion algorithm to estimate a final susceptibility map. Three healthy volunteers and three hemophilic patients were recruited to evaluate the UTE-QSM technique's ability to assess hemosiderin in the knee or ankle joint at 3T. One patient subsequently underwent total knee arthroplasty after the MR scan. The synovial tissues harvested from the knee joint during surgery were processed for histological analysis to confirm iron deposition.

Results: UTE-QSM successfully yielded tissue susceptibility maps of joints in both volunteers and patients. Multiple regions with high susceptibility over 1 ppm were detected in the affected joints of hemophilic patients, while no salient regions with elevated susceptibility were detected in asymptomatic healthy volunteers. Histology confirmed the presence of iron in regions where high susceptibility was detected by UTE-QSM.

*Corresponding Author: Jiang Du, Ph.D., jiangdu@ucsd.edu, University of California San Diego, Department of Radiology, 200 West Arbor Drive, San Diego, CA 92103-8226, Phone (619) 471-0519 | Fax (619) 471-0503.

DISCLOSURES

None

Conclusion: The UTE-QSM technique can detect hemosiderin deposition in the joint, and provides a potential sensitive biomarker for the diagnosis and prognosis of hemophilic arthropathy (HA).

Keywords

Hemophilia; UTE; QSM; Susceptibility; Arthropathy; Knee; Ankle

INTRODUCTION

Hemophilia is an X-linked bleeding disorder, characterized by deficiency of clotting factors VIII or IX and affecting approximately 25 out of every 100,000 live male births (1). Recently, the life expectancy of hemophilic patients has increased due to the development of virally safe clotting factors. Age-related comorbidities of the disease such as osteoarthritis (OA) have become a major focus in the care of hemophilic patients (2). In particular, many hemophilic patients suffer from frequent joint bleeding, which commonly begins in childhood and results in debilitating arthropathy caused by toxic iron depositions (i.e., hemosiderin) in synovium and cartilage. Frequent manifestations of iron-induced arthropathy are painful inflammatory synovial hypertrophy and osteochondral degeneration leading to subclinical joint bleeding (3). The development of a non-invasive biomarker sensitive to these changes in the joint is therefore of high importance to optimize efficacy of costly treatment plans and to improve monitoring progression of the disease.

The contemporary methods for radiological assessment of hemophilic arthritis (HA) include musculoskeletal ultrasound (MSK-US) (4,5) and MSK magnetic resonance imaging (MSK-MRI) (6,7). However, the question of which imaging technique is more efficient in the diagnosis of HA is up for debate. Recent development of high frequency MSK-US has enabled imaging of MSK tissues at higher spatial resolution, a potential advantage over MSK-MRI in terms of cost, patient comfort, and availability. However, MSK-US is limited in the penetration power and cannot accurately access deep regions such as the osteochondral junction. Furthermore, MSK-US imaging is highly dependent on the operator, making it a less reliable method in terms of providing objective and reproducible biomarkers of HA (8).

MSK-MRI provides high resolution structural information on human joints with excellent soft tissue contrast. Moreover, recent advancements in quantitative MSK-MRI techniques including MR relaxometry (T1, T2, T2*, and T1ρ) (9–12), diffusion weighted imaging (DWI) (13,14), quantitative susceptibility mapping (QSM) (15–18), and magnetization transfer (MT) imaging (19) have led to the development of sensitive biomarkers for OA, which may be useful in the diagnosis of HA due to their frequent comorbidity. Among these MSK-MRI techniques, QSM has emerged as a promising technique that allows characterization of tissues based on their magnetic susceptibilities. For example, iron is a paramagnetic element which generates a strong local magnetic field parallel to the applied magnetic field. By estimating the pixel-wise susceptibility in an MR system, the distribution of targeted particles can be estimated. In the literature, QSM has been investigated extensively in neuro (20–22), body (23,24), cardiovascular (25), and MSK imaging (15–18).

QSM may be a promising technique for HA, given its ability to quantify iron level in tissues. Its application in HA diagnosis would permit quantification of hemosiderin deposition without administration of exogenous contrast agent. Unfortunately, currently available clinical QSM techniques are limited in their detection range for magnetic susceptibilities in tissues since T2* shortens as iron concentration increases. Therefore, while regions with highly concentrated hemosiderin depositions are of critical importance in diagnosing HA, they pose a challenge to conventional MR imaging techniques due to their very short T2* values. Ultrashort echo time (UTE) sequences with echo times (TEs) ~100 times shorter than TEs of conventional sequences can detect signal from these short T2 tissues. UTE-based QSM (UTE-QSM) has been proposed as a way to evaluate susceptibilities of phantoms with highly concentrated iron nanoparticles (18,26,27). UTE MRI rapidly captures the free induction decay signal by minimizing the time delay between RF excitation and readout. In UTE MRI, the typical rewinding and/or phase encoding gradients used to prepare for data readout in conventional clinical Cartesian imaging are removed, and a center-out radial or spiral sampling strategy is utilized instead (28). The combination of UTE MR imaging and QSM analysis has allowed estimation of susceptibilities of short T2* tissues such as cortical bone, tendon, and ligament (17,18). However, it is unclear whether the UTE-QSM technique can be used to estimate susceptibility of hemosiderin in the joints of patients with HA.

In this study, we investigate the feasibility of using UTE-QSM to characterize hemosiderin deposition as a sensitive biomarker for HA. Three healthy volunteers and three hemophilic patients were recruited to evaluate the feasibility of the UTE-QSM technique in assessing hemosiderin in the knee or ankle joint at 3T. One patient underwent total knee arthroplasty after MR imaging. The synovial tissues harvested from the knee joint during surgery were processed for histological analysis to confirm iron deposition.

METHODS

3D UTE Cones Sequence

In this study, a 3D dual-echo UTE Cones sequence as shown in Figure 1A was utilized for data acquisition. The 3D UTE Cones sequence was implemented on a 3T clinical MR system (MR750, GE Healthcare, Milwaukee, WI, US). Either an 8-channel knee coil or an 8-channel ankle coil was used for signal excitation and transmission. UTE images at the minimum TE (TE1) were acquired by placing a center-out readout gradient immediately after RF coil deadtime—the part of the process where the RF coil switched from transmit to receive—of 32 μs. The second echo (TE2) images were acquired with a gradient recalled echo (GRE) imaging scheme. To acquire images at different TE1s and TE2s, the 3D dual-echo UTE Cones data were acquired with preset readout gradient delays. Figure 1B shows the readout trajectory, where the 3D k-space is encoded by spiral trajectories on the conical surfaces, a more time-efficient approach than 3D radial encoding (29,30).

Imaging Subjects

To test the proposed UTE-QSM sequence and processing pipeline, three healthy volunteers (three males, 35, 34, and 35 years old) and three hemophilic patients (three males, 28, 33,

and 37 years old, respectively) with HA were recruited in accordance with the Human Research Protection Program (HRPP) of University of California, San Diego. Signed consents were acquired from all six subjects before their involvement in the study. All three healthy volunteers and two of the three hemophilic patients underwent knee imaging (Patient A: 28-year-old and Patient B: 33-year-old), while the third hemophilic patient underwent ankle imaging (Patient C: 37-year-old). Patient A had moderate hemophilia (type A), while Patients B and C had severe hemophilia (type A). Severe and moderate Hemophilia A were defined by FVIII plasma activity of less than 1% and 1–5%, respectively. The affected joints of the three hemophilic patients were assessed using the Hemophilia Joint Health Score (HJHS, 0 being best, 20 being worst) (31).

MR Imaging

The knee MRI was performed with the following imaging parameters: 1) UTE-QSM: GE 8-channel transmit/receive knee coil, axial plane, flip angle (FA) = 15°, field of view (FOV) = 160×160×140 mm^3, acquisition matrix = 160×160×100; readout bandwidth (rBW) = 250 kHz, length of cones spiral arm = 848 μs, TR = 10 ms, three dual-echo scans (TE = 0.032/2.8, 0.2/3.6, and 0.4/4.4 ms), and total scan time = 18 min; 2) T1-weighted fast spin echo (FSE): sagittal plane, FOV = 160×160 mm^2, acquisition matrix = 512×512, number of slices = 50, slice thickness = 3 mm, rBW = 83.3 kHz, TR = 791 ms, TE = 8.0 ms, and total scan time = 2 min 45 sec; 3) T2-weighted FSE: GE standard fat saturation, sagittal plane, FOV = 160×160 mm^2, acquisition matrix = 512×512, number of slices = 50, slice thickness = 3 mm, rBW = 83.3 kHz, TR = 8728 ms, TE = 70.6 ms, and total scan time = 3 min 4 sec.

The ankle MRI was performed with the following imaging parameters: 1) UTE-QSM: GE 8-channel transmit/receive ankle coil, sagittal plane, FA = 15°, FOV = 160×160×140 mm^3, acquisition matrix = 160×160×100; rBW = 250 kHz, length of cones spiral arm = 848 μs, TR = 10 ms, three dual-echo scans (TE = 0.032/2.8, 0.2/3.6, and 0.4/4.4 ms), and total scan time = 18 min; 2) T1-weighted FSE: sagittal plane, FOV = 160×160 mm^2, matrix = 512×512, number of slices = 30, slice thickness = 3 mm, rBW = 83.3 kHz, TR = 601 ms, TE = 9.4 ms, and total scan time = 2 min 40 sec; 3) T2-weighted FSE: GE standard fat saturation, sagittal plane, FOV = 160×160 mm^2, acquisition matrix = 512×512, number of slices = 30, slice thickness = 3 mm, rBW = 83.3 kHz, TR = 6063 ms, TE = 74.2 ms, and total scan time = 3 min 48 sec.

Histology

Patient A underwent total knee arthroplasty after MR imaging on the same day. Surgery yielded multiple pieces of bone tissue from the femur, patella, and tibia, including some attached hypertrophic synovium. The tissues were fixed in 10% formalin (3.7% formaldehyde) for 48 hours and decalcified in 10% formic acid including 0.2% $K_4Fe(CN)_6$ to allow the Perl's reaction during decalcification (32). Resulting tissue was stained blue in iron-rich locations and was dehydrated and embedded in paraffin. 6–8 micron sections were counterstained with hematoxylin under acidic conditions for a red nuclear counterstain, and imaged on an Olympus AH-2 microscope with a 2.5X objective.

Data Processing

All non-clinical images were reconstructed from raw data acquired from the scanner, by using offline 3D gridding-based reconstruction implemented in Matlab R2017b (Mathworks, Natick, MA). Density function for the encoded k-space data was analytically estimated based on the distance to neighboring data points in the k-space. Gridding was performed using a Non-uniform Fast Fourier Transform (NuFFT) algorithm (33). The following gridding parameters were used: oversampling rate = 2 and kernel width = 5. The images reconstructed in the individual channels were combined to form a complex image (34). After channel combination (or coil combination), image registration utilizing a rigid registration algorithm based on affine transform provided in Matlab R2017b was performed to reduce errors caused by inter-scan motion. The magnitude images were used to find the affine transform matrix for individual images at different TEs with respect to the reference image at the first TE. The estimated transform matrix was separately applied to the real and imaginary images at other TEs to obtain a set of registered complex images, where cubic interpolation technique (35) was applied to generate the registered images.

T2* was estimated for demonstration purposes in a region of interest (ROI) of Patient A, where the mean signal of the manually drawn ROI was fitted using a non-linear optimization method based on the Levenberg-Marquardt algorithm implemented in Matlab R2017b.

Quantitative Susceptibility Mapping

After image reconstruction, coil combination, and image registration, the resulting complex MR images acquired using the UTE Cones sequence at six TEs (TE = 0.032, 0.2, 0.4, 2.8, 3.6, and 4.4 ms) were input to the Iterative Decomposition of water and fat with Echo Asymmetry and Least-squares estimation (IDEAL) framework (36). The IDEAL framework in UTE-QSM data processing was established utilizing Fat-Water Toolbox (version 1) which was initially developed as an initiative of the International Society of Magnetic Resonance in Medicine (ISMRM) Fat-Water MRI Workshop 2012 (37). Of the various fat-water separation methods provided in this toolbox, this study utilized the ‘multi-point fat-water separation with R2* using a graphcut field map estimation’ algorithm developed by Hernando et al. (38). The initial guess of field map for IDEAL was calculated by simple least square linear fitting based on the echo time and phase evolution without consideration of chemical shift. The estimated global field map was input to the subsequent QSM pipeline, which was composed based on Morphology-Enabled Dipole Inversion (MEDI) Toolbox. First, the projection onto dipole field (PDF) algorithm was applied to acquire a local field map (39). Then, the resultant local field map was input to the MEDI QSM algorithm to estimate the final susceptibility map (40). The MEDI-QSM algorithm was performed with Lagrange multiplier of 30000. No additional reference tissue was used, and the susceptibility values were intrinsically referenced to a zero-average value over the 3D data set in the QSM processing.

To process the input images with IDEAL and MEDI-QSM, a 3D mask for object region was used to exclude background. The mask was generated based on an averaged magnitude image of all six input images at different TEs, where pixelwise thresholding was performed to select the object region (at least 10% of the maximum signal intensity in the averaged

image), followed by a slice-by-slice 2D hole-filling algorithm ('imfill' function in Matlab). B_0 direction and the center frequency as well as other imaging parameters required for QSM processing were extracted from the raw data header file.

RESULTS

Healthy Volunteers

Figure 2 shows the susceptibility maps obtained using the proposed UTE-QSM method for three heathy volunteers (Figure 2A: 35-year-old, Figure 2B: 34-year-old, and Figure 2C: 35-year-old male) reformatted to the sagittal plane. Overall, the susceptibility values were estimated to be less than ~0.5 ppm, where most tissues exhibit negative susceptibility (i.e., diamagnetic). No localized regions of high susceptibility were detected.

Hemophilic Patients

The HJHS evaluated for the affected knee or ankle joints of Patients A, B, and C were 12, 11, and 4, respectively.

Figure 3 shows the magnitude (Figure 3A) and phase images (Figure 3B) of Patient A acquired with six different TEs. The regions indicated by red arrows in Figure 3A show a rapid signal decay, with near zero signal at later TEs (i.e., 2.8, 3.6, and 4.4 ms), presumably due to the accumulated hemosiderin present in the imaged joint. Figure 3C demonstrates rapid signal decay (right) for an ROI indicated by a yellow dotted line in the magnitude image (left) at TE of 32 μs. The estimated T2* in the ROI is 0.36 ± 0.06 ms. The R2* map acquired from IDEAL is shown in the middle of Figure 3C.

Figures 4A and 4B show the estimated water and fat images from IDEAL. Signal from the hemosiderin regions is present in the water image, while it is not in the estimated fat image (red arrows). In some pixels with extremely high iron, it was seen the signal is nulled in both the water and fat images, which is presumably due to the extremely short T2* limiting attainable signal-to-noise ratio (SNR) even in the UTE-QSM with a minimum TE of 32 μs. Figure 4C shows a total field map estimated using IDEAL, which shows the global B_0 inhomogeneity expressed in hertz. Figure 4D shows a local field map, which was obtained by removing background field using the PDF algorithm. The resultant susceptibility map estimated using the MEDI-QSM algorithm is shown in Figure 4E, where high susceptibility values were detected in multiple regions, as indicated by yellow arrows corresponding to regions with rapid signal decay observed in the magnitude images of Figure 3A.

Figure 5 shows clinical MR images and UTE-QSM results obtained from all three hemophilic patients, reformatted to the sagittal plane. Increased susceptibility was detected in the resultant susceptibility maps. The estimated susceptibilities for ROIs indicated by white arrows were 4.9 ± 2.5 ppm, 2.4 ± 1.6 ppm, and 2.3 ± 1.9 ppm for Patients A, B, and C, respectively.

Histology

Figures 6A and 6C show two representative slices selected from 3D UTE-QSM susceptibility maps for Patient A, who underwent total knee replacement surgery. The iron-

rich synovial tissue that adhered to the harvested bone included two sites, designated Tissue A and Tissue B, which correspond to white arrows in Figures 6A and 6C, respectively. Figures 6B and 6D show the corresponding histology images for Tissue A and Tissue B, respectively, with arrows highlighting areas of intense iron deposition (Perl's reaction product, Prussian Blue). Tissue A showed more areas of intense blue than Tissue B, although both tissues showed noticeably intense blue in vesicle-like globules and in diffuse extracellular distribution. In UTE-QSM, the estimated susceptibility for the corresponding region where Tissue A was harvested from was 4.5 ± 1.8 ppm. The estimated susceptibility for the corresponding region where Tissue B was harvested from was 2.7 ± 1.1 ppm, demonstrating lower susceptibility than Tissue A consistent with histological iron staining.

DISCUSSION

HA is a major concern for patients with hemophilia, causing pain, disability, and an overall decrease in quality of life. It is well known that spontaneous joint bleeding may lead to arthropathy due to the toxic environment in the synovium induced by the increased hemosiderin deposition. Early prophylactic treatment with clotting factor replacement to avoid the development of "target joints" (i.e., joints which experience consecutive bleeding within a six month period) can greatly reduce progression to HA (41). However, it has also been reported that approximately 30–50% of patients who have been administered prophylaxis since childhood still suffer from arthropathy (42–44). Unfortunately, the mechanism underlying HA is not entirely understood, and asymptomatic bleeds and toxic iron accumulation may fuel joint deterioration. Therefore, a sensitive, non-invasive biomarker is urgently needed to provide a more in-depth understanding of the pathogenesis of HA, as well as to provide vital disease monitoring information that can be used in tandem with targeted treatment plans to slow down, or even prevent, HA. In this study, we focused on the application of the novel UTE-QSM technique in detection of hemosiderin deposition in the joints of hemophilic patients with arthropathy.

In the in vivo experiment, hemophilic patients showed several localized regions in the joints (Figure 5) with high susceptibility (> 1 ppm) in this study. In the histological experiment performed on the harvested synovial tissues from the knee joint of Patient A, more densely concentrated iron was detected in the region exhibiting higher susceptibility, as shown in Figure 6, which demonstrates the quantitative nature of the proposed UTE-QSM method. Interestingly, despite the similar HJHS (12 for Patient A and 11 for Patient B), much higher susceptibility was detected in the knee joint of Patient A than Patient B. In future investigations the correlation between QSM and clinical scores including HJHS will be investigated further with a larger number of patients. We will also consider the possibility of different HA phenotypes, addressing relevant clinical factors such as hemophilia type and severity.

There were several factors to consider in order to achieve a reliable quantitative biomarker based on QSM in hemophilia. First, unlike QSM of the brain, which is the most common QSM application and where the tissue susceptibility in normal or abnormal brain is commonly less than ~0.2 ppm (20–22), we were confronted with trying to detect susceptibility values up to 40-magnitude higher (~8 ppm) in our investigation of HA. Due to

the ultra-high magnetic susceptibility and the consequent extremely short T2*, it was necessary to utilize UTE imaging to resolve MR signal in these regions with high iron concentrations. Second, off-resonance effect from the chemical shift of lipid was a critical issue to address for QSM evaluation of the knee or ankle joint, as it can hamper accurate estimation of the B_0 field map and the resultant susceptibility mapping. The simplest way to resolve this consideration is to acquire MR images at TEs where fat and water signals are in-phase so that the off-resonance effect can be neglected (e.g., TEs near 2.2 or 4.4 ms at 3T). Unfortunately, this approach is not applicable to QSM in hemophilia due to the extremely short T2* associated with high iron concentration. As a result, MR signal decays quickly to near-noise levels at later TEs, where no phase information is available, as demonstrated in Figure 3B. The interleaved dual-echo 3D UTE-Cones data acquisition scheme can accurately detect the phase evolution for hemosiderin, while the IDEAL processing can reliably separate fat and water, providing robust phase information in the presence of fat. Therefore, in this study we utilized the UTE-IDEAL framework to resolve the aforementioned challenges associated with hemosiderin and fat, providing accurate estimation of the B_0 field map for joints of hemophilia patients.

Streaking artifact and bias in the susceptibility map are a potential concern which may hamper accurate estimation of susceptibility especially for the regions with low iron level. Particularly in HA, hemosiderin that is highly concentrated in multiple local regions may generate a strong local field, causing streaking artifacts in QSM. Moreover, in the current QSM framework based on IDEAL, any errors in the total field map, such as spatial noise in the input images or uncorrected motion between the images at different TEs, can also cause streaking artifacts. Low frequency bias was also observed in the estimated susceptibility maps (Figures 5F and 5I, and Figure 6A), which may result from several factors such as bias in the source image that can be propagated due to the sub-optimal regularization in MEDI processing and imperfect background field removal.

In addition, the phase evolution during the readout can be a source of error in IDEAL and QSM processing. The blurring and ringing artifacts due to off-resonance combined with Cones trajectory can be confounding factors. Though these artifacts may affect phase in Cones images at different TEs, the phase error is expected to be similar across all images since we have utilized a fly-back multi-echo scheme where the k-space trajectories are kept the same for all TEs. When considering the phase evolution (i.e., phase differences between TEs), the initial phase errors can be neglected. Therefore, we expect that the QSM results are not significantly affected by readout duration of the spiral arm. In a related investigation, we have recently reported the readout duration (length of spiral arm) in Cones UTE imaging (26).

In our previous phantom studies, we demonstrated the ability of UTE-QSM to quantify iron concentration by showing an excellent linear relationship between UTE-QSM and iron concentrations up to 22 mM, which corresponds to an R2* of 5 ms^{-1} or T2* of 200 μs (27). Given the nominal shortest TE of around ~32 μs (due to the RF coil T/R switch time) of the UTE sequence in modern clinical MR systems, it is challenging to resolve signals from higher iron levels with extremely short T2*s (< 100 μs), especially in IDEAL processing as shown in Figures 4A and 4B. Short T2* blurring is known to be an inevitable issue in UTE

imaging, and also therefore affects UTE-QSM. Although we did not observe significant errors in susceptibility maps due to short T2* blurring or ringing artifacts around the vials with high iron concentrations in our previous experiments (18,26,27), this hardware limitation poses a technical challenge for UTE-QSM sensitivity to tissues with lower iron concentrations in HA.

There were relatively strong artifacts in the ankle QSM maps as shown in Figure 5i, which may have been caused by a number of factors including the strong susceptibility source in ankle imaging (i.e., irregular shape), large anisotropic voxel size, inter- and intra-scan motion during the relatively long data acquisition time, relatively low SNR, and sub-optimal regularization in MEDI-QSM data processing. Those factors are likely to affect tissues with lower susceptibilities (e.g., muscle) more than hemosiderin-rich tissues. The proposed framework for UTE-QSM processing of HA needs further investigation including the optimization of imaging (e.g., spatial resolution, echo spacing, calibration for effective TE, and the longest TE) and data processing (e.g., regularization parameters in MEDI) and better motion registration technique (e.g., advanced normalization tools (45)). Recently, many QSM algorithms based on different strategies have been proposed to solve the ill-conditioned dipole inversion problem (40). In future studies, we will investigate the combination of the interleaved dual-echo UTE Cones data acquisition scheme with new QSM algorithms, such as the streaking artifact reduction for QSM (STAR-QSM) algorithm (46) and the improved sparse linear equation and least-squares (iLSQR) algorithm (47) in the evaluation of HA. We will also try different background field removal algorithms such as the spherical mean value (SMV) filtering algorithm (48).

Beyond this feasibility study, there is a need to systematically investigate the quantification accuracy of the proposed UTE-QSM method in HA by performing biochemical and histological analyses of harvested tissues from different regions of the hemophilic joint as ground truth. It is also necessary to recruit a larger number of hemophilic patients to evaluate the proposed biomarker based on UTE-QSM in correlation with other conventional MR imaging techniques. It is important to measure all available MR parameters including susceptibility, T1, T2*, T1ρ, and MT in HA. It will also be interesting to investigate different phenotypes in HA compared with OA (without hemophilia) using these techniques. Moreover, it is important to set up a reference tissue to correct for inter-subject offsets in susceptibility in a large-scale in vivo study of hemophilia patients and healthy controls. The current implementation of UTE-QSM without a reference tissue may cause more issues in MSK imaging than in brain imaging when making comparisons of susceptibility values across data sets because of the greater variability of the anatomy and larger range of susceptibility values. This remains to be investigated in depth. Ultimately, we hope that 3D UTE-QSM assessment of hemosiderin, together with other MRI biomarkers, may provide an effective tool for more comprehensive and accurate assessment of HA, as well as for improved management of decisions regarding bleed prevention strategies.

CONCLUSIONS

We demonstrated the feasibility of 3D UTE-QSM in detecting hemosiderin accumulation in the joints of hemophilic patients, providing a potential sensitive biomarker for toxic iron accumulation in joints to improve the diagnosis and treatment of hemophilic arthropathy.

ACKNOWLEDGEMENTS

The authors acknowledge grant support from the NIH (R01 AR075825, 2R01 AR062581, 1R01 NS092650, and 1R01 AR068987), VA Clinical Science and Rehabilitation Research and Development Services (Merit Awards I01CX001388 and I01RX002604), Health Resource and Service Agency (H30MC24045), and GE Healthcare.

REFERENCES

1. Iorio A, Stonebraker JS, Chambost H, et al. Establishing the Prevalence and Prevalence at Birth of Hemophilia in Males. Ann. Intern. Med 2019;171:540 doi: 10.7326/M19-1208. [PubMed: 31499529]
2. Darby SC, Kan SW, Spooner RJ, et al. Mortality rates, life expectancy, and causes of death in people with hemophilia A or B in the United Kingdom who were not infected with HIV. Blood 2007;110:815–825 doi: 10.1182/blood-2006-10-050435. [PubMed: 17446349]
3. van Vulpen LFD, Holstein K, Martinoli C. Joint disease in haemophilia: Pathophysiology, pain and imaging. Haemophilia 2018;24:44–49 doi: 10.1111/hae.13449. [PubMed: 29878659]
4. Ceponis A, Wong-Sefidan I, Glass CS, von Drygalski A. Rapid musculoskeletal ultrasound for painful episodes in adult haemophilia patients. Haemophilia 2013;19:790–798 doi: 10.1111/hae.12175. [PubMed: 23672827]
5. Kidder W, Nguyen S, Larios J, Bergstrom J, Ceponis A, von Drygalski A. Point-of-care musculoskeletal ultrasound is critical for the diagnosis of hemarthroses, inflammation and soft tissue abnormalities in adult patients with painful haemophilic arthropathy. Haemophilia 2015;21:530–537 doi: 10.1111/hae.12637. [PubMed: 25623830]
6. Feldman BM, Funk S, Lundin B, Doria AS, Ljung R, Blanchette V. Musculoskeletal measurement tools from the International Prophylaxis Study Group (IPSG). Haemophilia 2008;14:162–169 doi: 10.1111/j.1365-2516.2008.01750.x. [PubMed: 18510537]
7. Chan MW, Leckie A, Xavier F, et al. A systematic review of MR imaging as a tool for evaluating haemophilic arthropathy in children. Haemophilia 2013;19:e324–e334 doi: 10.1111/hae.12248. [PubMed: 23919318]
8. Soliman M, Daruge P, Dertkigil SSJ, et al. Imaging of haemophilic arthropathy in growing joints: pitfalls in ultrasound and MRI. Haemophilia 2017;23:660–672 doi: 10.1111/hae.13249. [PubMed: 28574216]
9. Biercevicz AM, Murray MM, Walsh EG, Miranda DL, Machan JT, Fleming BC. T2* MR relaxometry and ligament volume are associated with the structural properties of the healing ACL. J. Orthop. Res 2014;32:492–499 doi: 10.1002/jor.22563. [PubMed: 24338640]
10. Li X, Benjamin Ma C, Link TM, et al. In vivo T1ρ and T2 mapping of articular cartilage in osteoarthritis of the knee using 3T MRI. Osteoarthr. Cartil. 2007;15:789–797 doi: 10.1016/j.joca.2007.01.011.
11. Ma YJ, Zhao W, Wan L, et al. Whole knee joint T 1 values measured in vivo at 3T by combined 3D ultrashort echo time cones actual flip angle and variable flip angle methods. Magn. Reson. Med 2019;81:1634–1644 doi: 10.1002/mrm.27510. [PubMed: 30443925]
12. Regatte RR, Akella SVS, Lonner JH, Kneeland JB, Reddy R. T1ρ relaxation mapping in human osteoarthritis (OA) cartilage: Comparison of T1ρ with T2. J. Magn. Reson. Imaging 2006;23:547–553 doi: 10.1002/jmri.20536. [PubMed: 16523468]
13. Wang N, Mirando AJ, Cofer G, Qi Y, Hilton MJ, Johnson GA. Diffusion tractography of the rat knee at microscopic resolution. Magn. Reson. Med 2019;81:3775–3786 doi: 10.1002/mrm.27652. [PubMed: 30671998]

14. Bieri O, Ganter C, Scheffler K. Quantitative in vivo diffusion imaging of cartilage using double echo steady-state free precession. Magn. Reson. Med 2012;68:720–729 doi: 10.1002/mrm.23275. [PubMed: 22161749]
15. Wang L, Nissi MJ, Toth F, et al. Quantitative susceptibility mapping detects abnormalities in cartilage canals in a goat model of preclinical osteochondritis dissecans. Magn. Reson. Med 2017;77:1276–1283 doi: 10.1002/mrm.26214. [PubMed: 27018370]
16. Wei H, Dibb R, Decker K, et al. Investigating magnetic susceptibility of human knee joint at 7 Tesla. Magn. Reson. Med 2017;78:1933–1943 doi: 10.1002/mrm.26596. [PubMed: 28097689]
17. Dimov AV, Liu Z, Spincemaille P, Prince MR, Du J, Wang Y. Bone quantitative susceptibility mapping using a chemical species-specific R2* signal model with ultrashort and conventional echo data. Magn. Reson. Med 2017;00 doi: 10.1002/mrm.26648.
18. Jang H, Lu X, Carl M, et al. True phase quantitative susceptibility mapping using continuous single-point imaging: a feasibility study. Magn. Reson. Med 2019;81:1907–1914 doi: 10.1002/mrm.27515. [PubMed: 30325058]
19. Grosse U, Syha R, Hein T, et al. Diagnostic value of T1 and T2* relaxation times and off-resonance saturation effects in the evaluation of achilles tendinopathy by MRI at 3T. J. Magn. Reson. Imaging 2015;41:964–973 doi: 10.1002/jmri.24657. [PubMed: 24817378]
20. Acosta-Cabronero J, Betts MJ, Cardenas-Blanco A, Yang S, Nestor PJ. In Vivo MRI Mapping of Brain Iron Deposition across the Adult Lifespan. J. Neurosci 2016;36:364–374 doi: 10.1523/JNEUROSCI.1907-15.2016. [PubMed: 26758829]
21. Barbosa JHO, Santos AC, Tumas V, et al. Quantifying brain iron deposition in patients with Parkinson's disease using quantitative susceptibility mapping, R2 and R2*. Magn. Reson. Imaging 2015;33:559–565 doi: 10.1016/j.mri.2015.02.021. [PubMed: 25721997]
22. Wisnieff C, Ramanan S, Olesik J, Gauthier S, Wang Y, Pitt D. Quantitative susceptibility mapping (QSM) of white matter multiple sclerosis lesions: Interpreting positive susceptibility and the presence of iron. Magn. Reson. Med 2015;74:564–570 doi: 10.1002/mrm.25420. [PubMed: 25137340]
23. Xie L, Dibb R, Cofer GP, et al. Susceptibility tensor imaging of the kidney and its microstructural underpinnings. Magn. Reson. Med 2015;73:1270–1281 doi: 10.1002/mrm.25219. [PubMed: 24700637]
24. Jafari R, Sheth S, Spincemaille P, et al. Rapid automated liver quantitative susceptibility mapping. J. Magn. Reson. Imaging 2019;50:725–732 doi: 10.1002/jmri.26632. [PubMed: 30637892]
25. Dibb R, Qi Y, Liu C. Magnetic susceptibility anisotropy of myocardium imaged by cardiovascular magnetic resonance reflects the anisotropy of myocardial filament α-helix polypeptide bonds. J. Cardiovasc. Magn. Reson 2015;17:60 doi: 10.1186/s12968-015-0159-4. [PubMed: 26177899]
26. Lu X, Jang H, Ma Y, Jerban S, Chang E, Du J. Ultrashort Echo Time Quantitative Susceptibility Mapping (UTE-QSM) of Highly Concentrated Magnetic Nanoparticles: A Comparison Study about Different Sampling Strategies. Molecules 2019;24:1143 doi: 10.3390/molecules24061143.
27. Lu X, Ma Y, Chang EY, et al. Simultaneous quantitative susceptibility mapping (QSM) and R2* for high iron concentration quantification with 3D ultrashort echo time sequences: An echo dependence study. Magn. Reson. Med 2018;79:2315–2322 doi: 10.1002/mrm.27062. [PubMed: 29314215]
28. Robson MD, Gatehouse PD, Bydder M, Bydder GM. Magnetic Resonance: An Introduction to Ultrashort TE (UTE) Imaging. J. Comput. Assist. Tomogr 2003;27:825–846 doi: 10.1097/00004728-200311000-00001. [PubMed: 14600447]
29. Gurney PT, Hargreaves BA, Nishimura DG. Design and analysis of a practical 3D cones trajectory. Magn. Reson. Med 2006;55:575–582 doi: 10.1002/mrm.20796. [PubMed: 16450366]
30. Wan L, Zhao W, Ma Y, et al. Fast quantitative 3D ultrashort echo time MRI of cortical bone using extended cones sampling. Magn. Reson. Med 2019;82:225–236 doi: 10.1002/mrm.27715. [PubMed: 30821032]
31. Hilliard P, Funk S, Zourikins N, et al. Hemophilia joint health score reliability study. Haemophilia 2006;12:518–525 doi: 10.1111/j.1365-2516.2006.01312.x. [PubMed: 16919083]

32. von Drygalski A, Barnes RFW, Jang H, et al. Advanced magnetic resonance imaging of cartilage components in haemophilic joints reveals that cartilage hemosiderin correlates with joint deterioration. Haemophilia 2019;25:851–858 doi: 10.1111/hae.13802. [PubMed: 31199035]
33. Fessler JA. On NUFFT-based gridding for non-Cartesian MRI. J. Magn. Reson 2007;188:191–195 doi: 10.1016/j.jmr.2007.06.012. [PubMed: 17689121]
34. Walsh DO, Gmitro AF, Marcellin MW. Adaptive reconstruction of phased array MR imagery. Magn. Reson. Med 2000;43:682–90 doi: 10.1002/(sici)1522-2594(200005)43:5<682::aid-mrm10>3.0.co;2-g. [PubMed: 10800033]
35. Keys R Cubic convolution interpolation for digital image processing. IEEE Trans. Acoust 1981;29:1153–1160 doi: 10.1109/TASSP.1981.1163711.
36. Reeder SB, Pineda AR, Wen Z, et al. Iterative decomposition of water and fat with echo asymmetry and least-squares estimation (IDEAL): Application with fast spin-echo imaging. Magn. Reson. Med 2005;54:636–644 doi: 10.1002/mrm.20624. [PubMed: 16092103]
37. Hu HH, Börnert P, Hernando D, et al. ISMRM workshop on fat-water separation: Insights, applications and progress in MRI. Magn. Reson. Med 2012;68:378–388 doi: 10.1002/mrm.24369. [PubMed: 22693111]
38. Hernando D, Kellman P, Haldar JP, Liang ZP. Robust water/fat separation in the presence of large field inhomogeneities using a graph cut algorithm. Magn. Reson. Med 2010;63:79–90 doi: 10.1002/mrm.22177. [PubMed: 19859956]
39. Liu T, Khalidov I, de Rochefort L, et al. A novel background field removal method for MRI using projection onto dipole fields (PDF). NMR Biomed. 2011;24:1129–1136 doi: 10.1002/nbm.1670. [PubMed: 21387445]
40. Wang Y, Liu T. Quantitative susceptibility mapping (QSM): Decoding MRI data for a tissue magnetic biomarker. Magn. Reson. Med 2015;73:82–101 doi: 10.1002/mrm.25358. [PubMed: 25044035]
41. Aledort LM, Haschmeyer RH, Pettersson H. A longitudinal study of orthopaedic outcomes for severe factor-VIII-deficient haemophiliacs. J. Intern. Med 1994;236:391–399 doi: 10.1111/j.1365-2796.1994.tb00815.x. [PubMed: 7931042]
42. Aznar JA, Lucia F, Abad-Franch L, et al. Haemophilia in Spain. Haemophilia 2009;15:665–675 doi: 10.1111/j.1365-2516.2009.02001.x. [PubMed: 19432921]
43. Schramm W, Gringeri A, Ljung R, et al. Haemophilia Care in Europe: the ESCHQoL study. Haemophilia 2012;18:729–737 doi: 10.1111/j.1365-2516.2012.02847.x. [PubMed: 22639833]
44. Baumgardner J, Elon L, Antun A, et al. Physical activity and functional abilities in adult males with haemophilia: a cross-sectional survey from a single US haemophilia treatment centre. Haemophilia 2013;19:551–557 doi: 10.1111/hae.12134. [PubMed: 23574421]
45. Tustison NJ, Cook PA, Klein A, et al. Large-scale evaluation of ANTs and FreeSurfer cortical thickness measurements. Neuroimage 2014;99:166–179 doi: 10.1016/j.neuroimage.2014.05.044. [PubMed: 24879923]
46. Wei H, Dibb R, Zhou Y, et al. Streaking artifact reduction for quantitative susceptibility mapping of sources with large dynamic range. NMR Biomed. 2015;28:1294–1303 doi: 10.1002/nbm.3383. [PubMed: 26313885]
47. Li W, Wang N, Yu F, et al. A method for estimating and removing streaking artifacts in quantitative susceptibility mapping. Neuroimage 2015;108:111–122 doi: 10.1016/j.neuroimage.2014.12.043. [PubMed: 25536496]
48. Li W, Wu B, Liu C. Quantitative susceptibility mapping of human brain reflects spatial variation in tissue composition. Neuroimage 2011;55:1645–1656 doi: 10.1016/j.neuroimage.2010.11.088. [PubMed: 21224002]

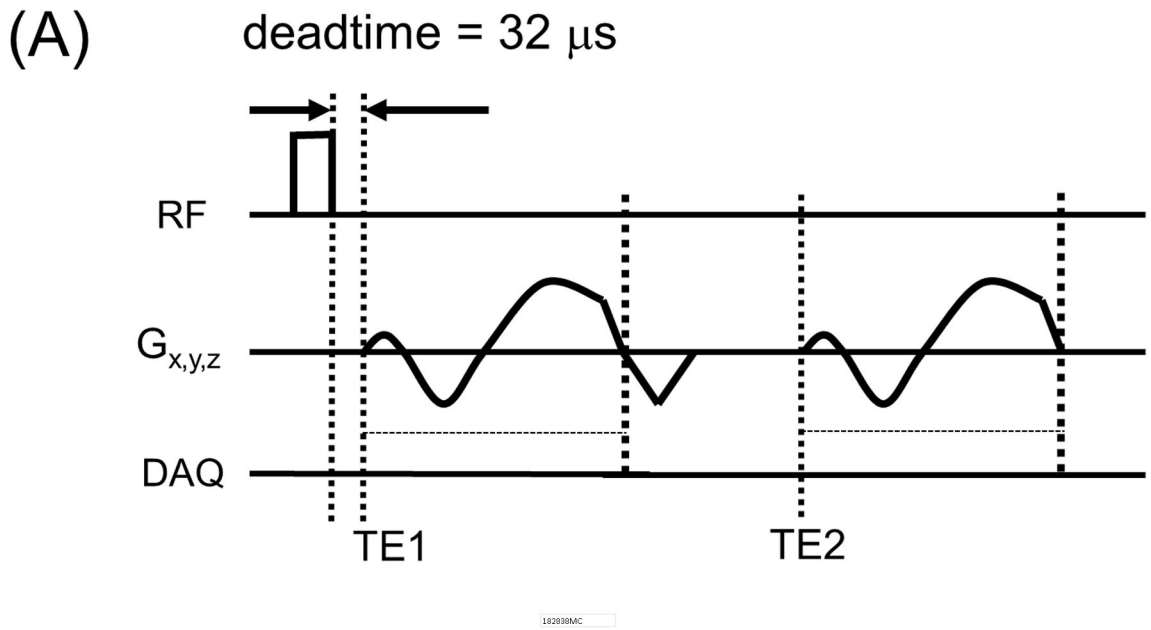

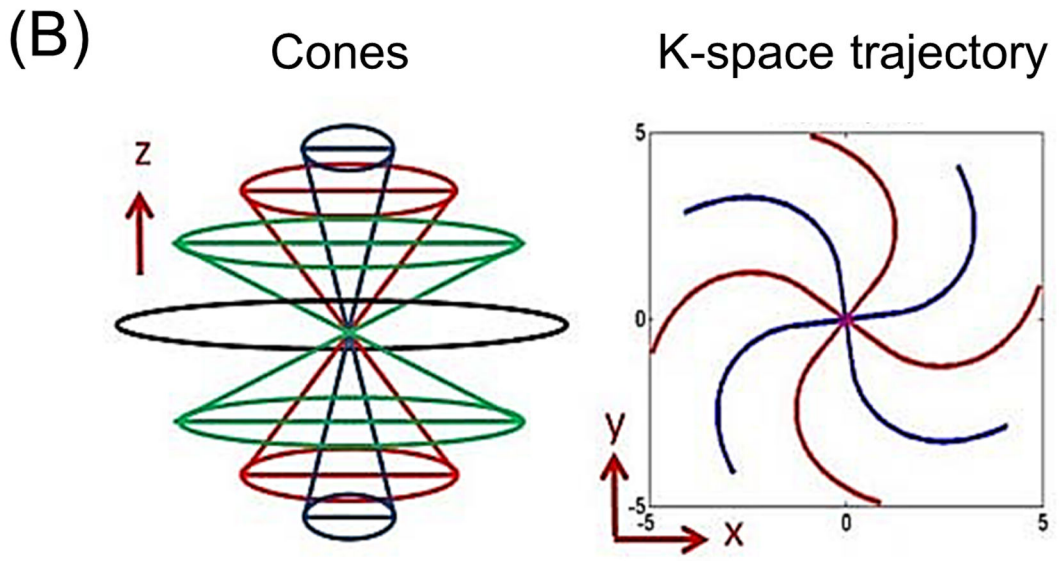

Figure 1.

3D dual-echo UTE Cones imaging. (A) Pulse sequence and (B) k-space trajectory. The dual-echo imaging is repeated to acquire multiple TEs (six in this study) at different TEs, TE1 and TE2, by delaying the readout gradient.

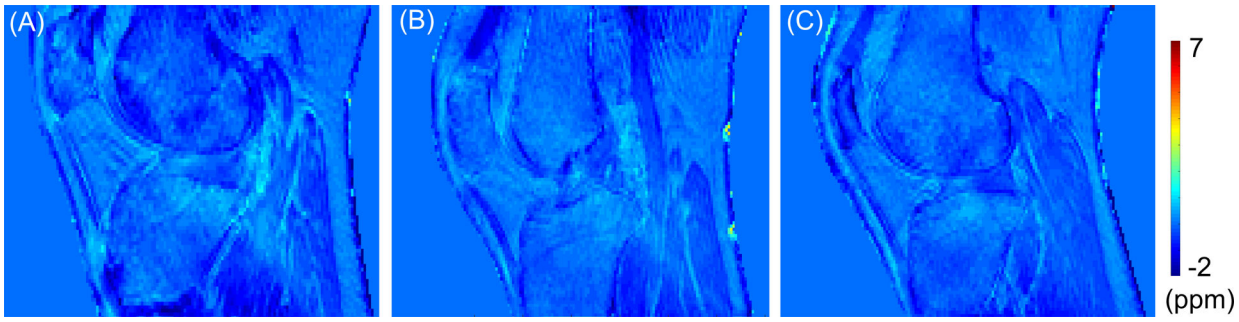

Figure 2.

Healthy volunteers (A: 35-year-old, B: 34-year-old, and C: 35-year-old male). The estimated susceptibility map shows very little spatial variation between tissues and no localized regions of high susceptibility.

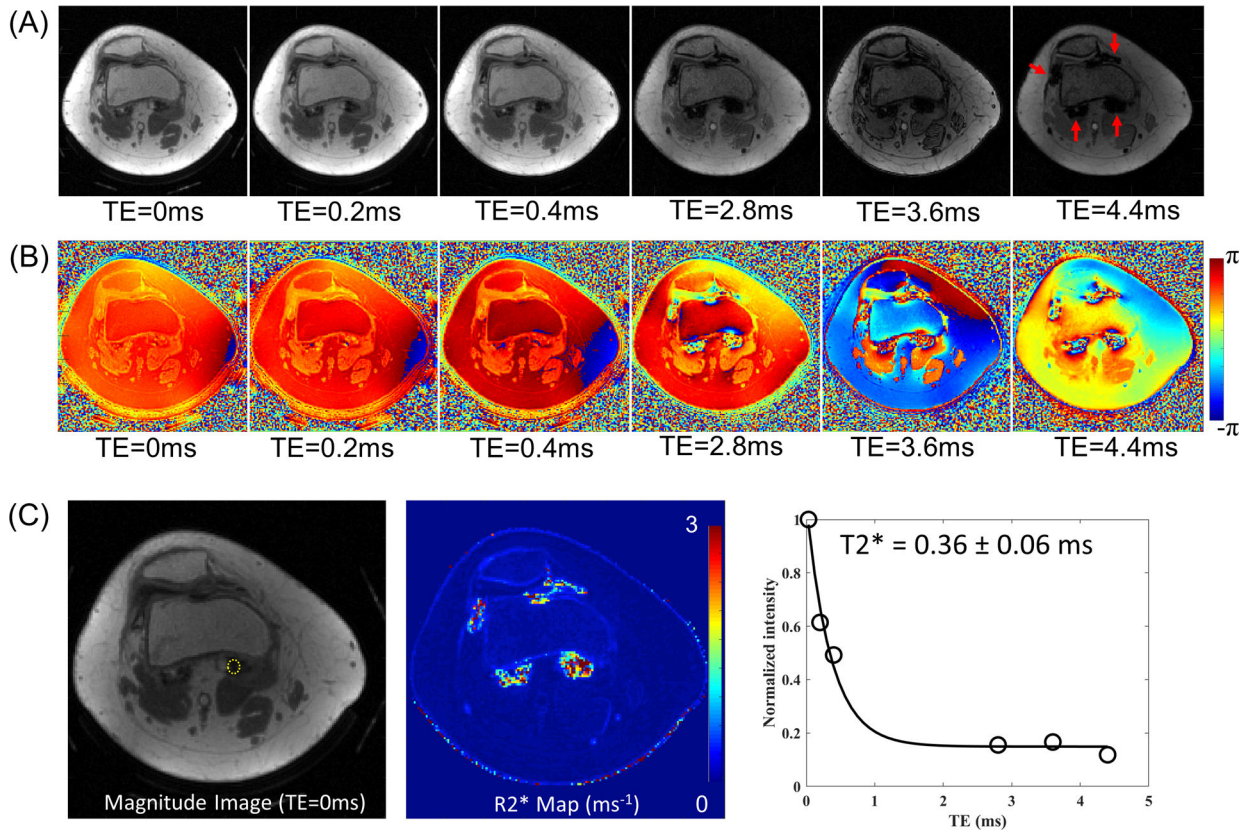

Figure 3.

Reconstructed images from Patient A. (A) Magnitude and (B) phase images, and (C) a region of interest (yellow dotted line) in magnitude image at TE of 32 μs (left), the estimated R2* map from IDEAL (middle), and signal decay and T2* estimation (right). Rapid signal decay is shown in the regions indicated by red arrows in (A), which is due to the highly concentrated hemosiderin. The measured T2* in one region (yellow circle in C) is 0.36 ± 0.06 ms, which is impossible to capture with clinical MR sequences with long TE.

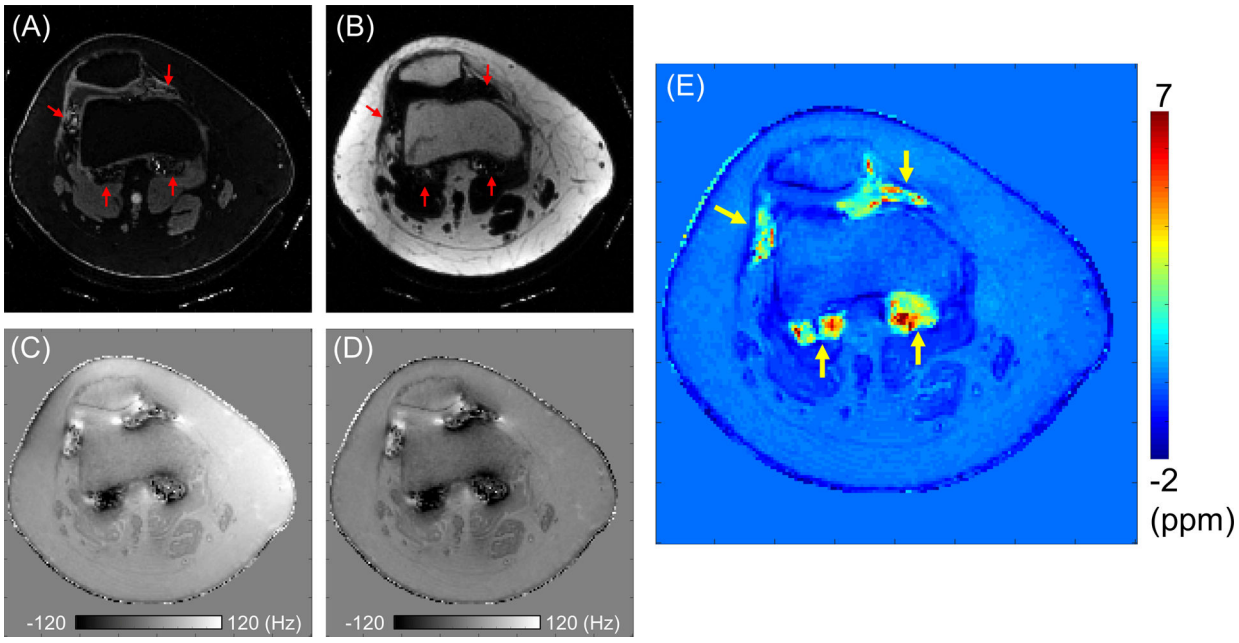

Figure 4.

QSM estimation in Patient A. (A) A water image, (B) a fat image, and (C) a total field map from IDEAL, (D) a local field map after PDF algorithm, and (E) the estimated susceptibility map. Signal from the hemosiderin regions is present in the water image, while it is not in the estimated fat image (red arrows). High susceptibility is detected in the regions indicated by yellow arrows.

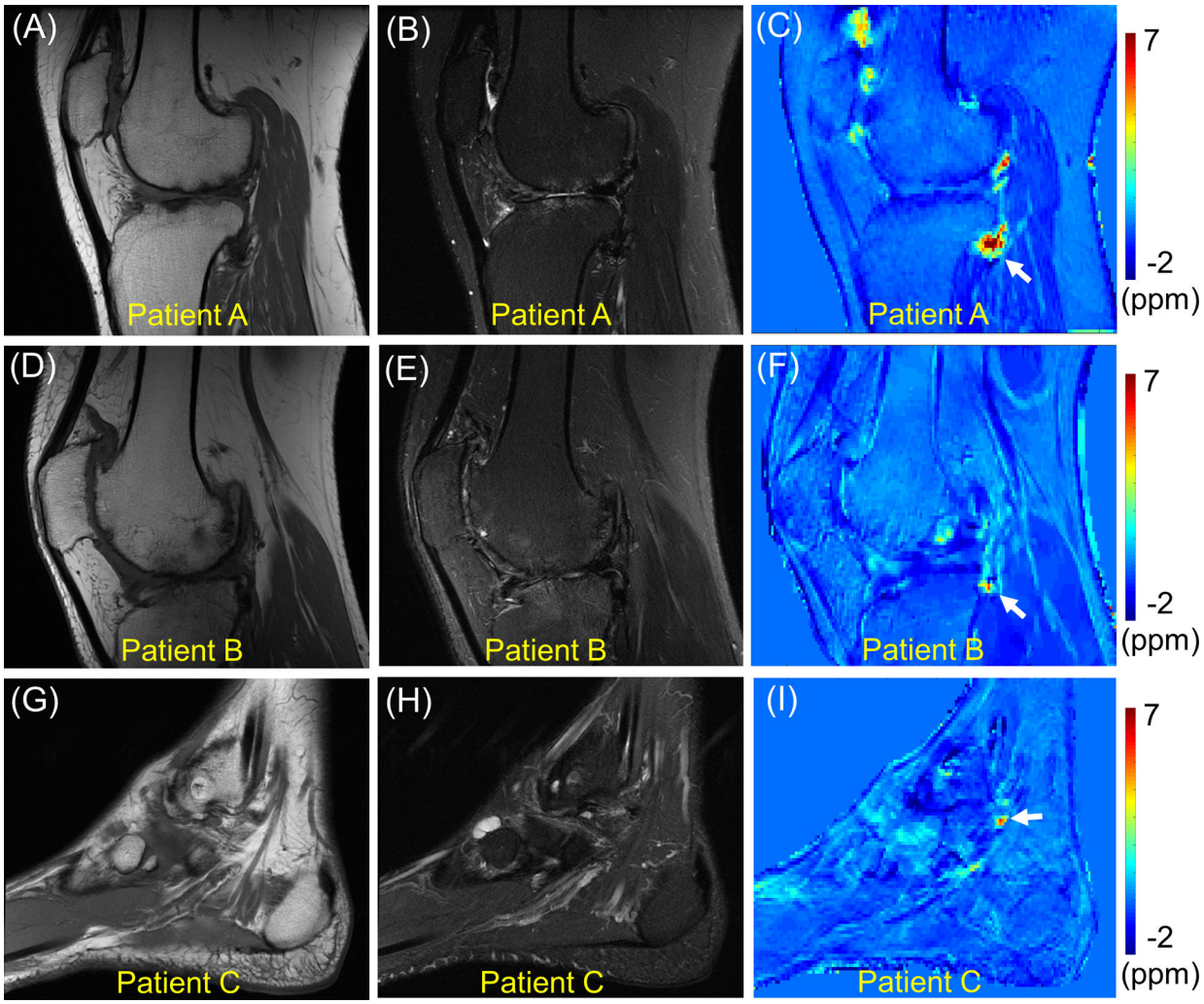

Figure 5.

Clinical MR images and QSM in all three hemophilic patients. T1-weighted MRI (A, D, G), T2-weighted MRI (B, E, H), and QSM (C, F, I). The susceptibility estimated in the regions of interest indicated by white arrows are 4.9 ± 2.5 ppm, 2.4 ± 1.6 ppm, and 2.3 ± 1.9 ppm for Patients A, B, and C, respectively.

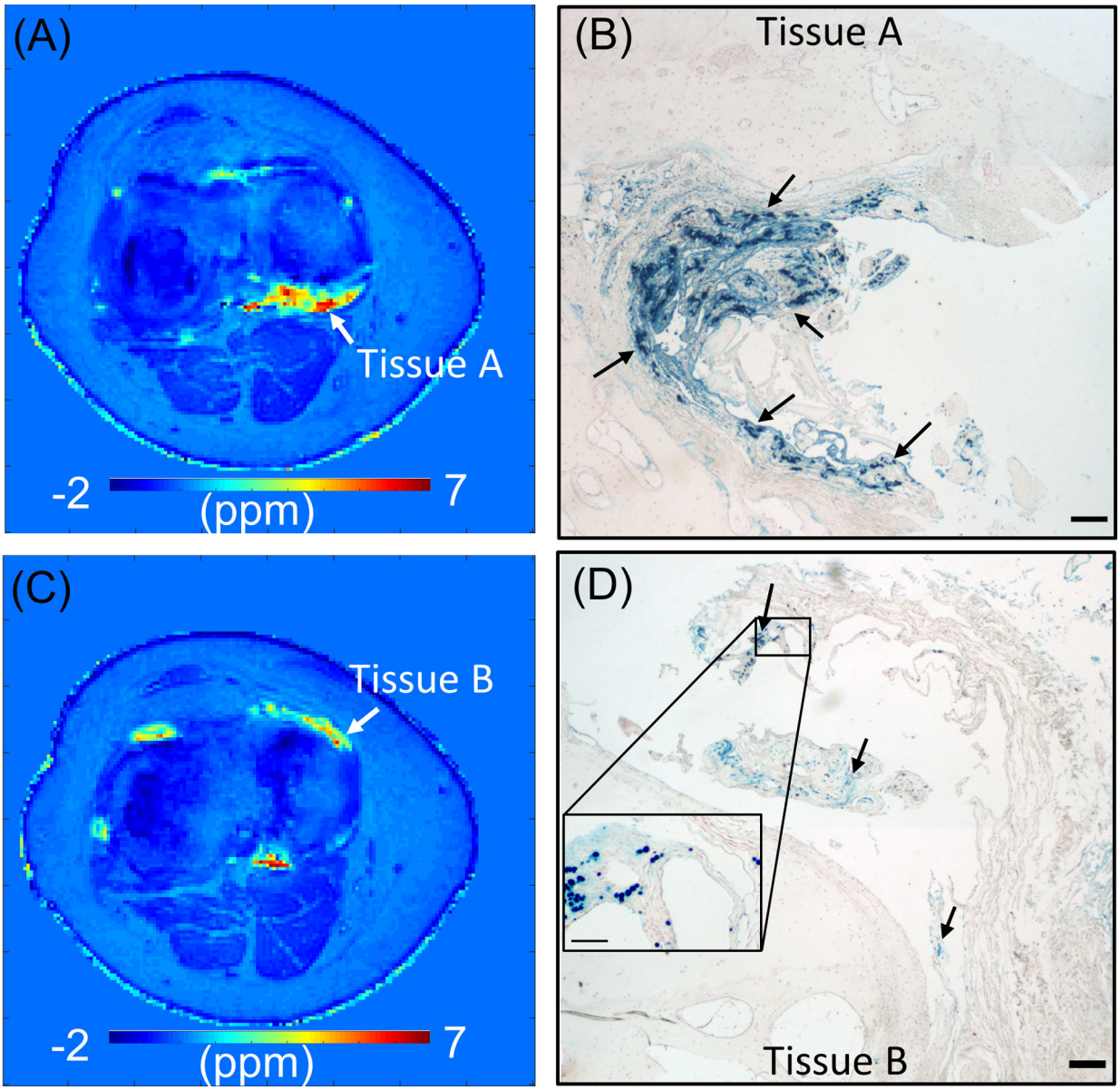

Figure 6.

Histology of osteochondral tissues from Patient A. Susceptibility map estimated in two representative slices (A and C) and the corresponding histological images (B and D). Perl's reaction product (blue) in B and D demonstrate iron (arrows) with a concentration-dependent intensity, primarily shown in hypertrophic synovial tissue adherent to the joint. Bars represent 200 microns in widefield images and 50 microns in insets. Red hematoxylin counterstain was applied. The measured susceptibility with UTE-QSM is 4.5 ± 1.8 ppm for Tissue A and 2.7 ± 1.1 ppm for Tissue B, which agrees with the observation that Tissue A shows higher iron concentration than Tissue B in histology.